

Strong, anisotropic anomalous Hall effect and spin Hall effect in chiral antiferromagnetic compounds Mn_3X ($X = Ge, Sn, Ga, Ir, Rh$ and Pt)

Yang Zhang,^{1,2} Yan Sun,¹ Hao Yang,^{1,3} Jakub Železný,¹ Stuart P. P. Parkin,³ Claudia Felser,¹ and Binghai Yan^{1,4,*}

¹Max Planck Institute for Chemical Physics of Solids, 01187 Dresden, Germany

²Leibniz Institute for Solid State and Materials Research, 01069 Dresden, Germany

³Max Planck Institute of Microstructure Physics, Weinberg 2, 06120 Halle, Germany

⁴Max Planck Institute for the Physics of Complex Systems, 01187 Dresden, Germany

We have carried out a comprehensive study of the intrinsic anomalous Hall effect and spin Hall effect of several chiral antiferromagnetic compounds, Mn_3X ($X = Ge, Sn, Ga, Ir, Rh$ and Pt) by *ab initio* band structure and Berry phase calculations. These studies reveal large and anisotropic values of both the intrinsic anomalous Hall effect and spin Hall effect. The Mn_3X materials exhibit a non-collinear antiferromagnetic order which, to avoid geometrical frustration, forms planes of Mn moments that are arranged in a Kagome-type lattice. With respect to these Kagome planes, we find that both the anomalous Hall conductivity (AHC) and the spin Hall conductivity (SHC) are quite anisotropic for any of these materials. Based on our calculations, we propose how to maximize AHC and SHC for different materials. The band structures and corresponding electron filling, that we show are essential to determine the AHC and SHC, are compared for these different compounds. We point out that Mn_3Ga shows a large SHC of about $600 (\hbar/e)(\Omega \cdot cm)^{-1}$. Our work provides insights into the realization of strong anomalous Hall effects and spin Hall effects in chiral antiferromagnetic materials.

I. INTRODUCTION

The anomalous Hall effect (AHE)¹ and spin Hall effect (SHE)² are very important members of the family of Hall effects. The AHE is characterized by a transverse voltage generated by a longitudinal charge current usually in a ferromagnetic (FM) metal. The AHE can be generalized to the case of the SHE in nonmagnetic materials in which Mott scattering³ leads to the deflection of spin-up and -down charge carriers in opposite directions, owing to spin-orbit coupling (SOC), as illustrated in Fig. 1. Thus, a longitudinal charge current can generate opposite spin accumulations along opposing edges in the transverse direction to the current. On the contrary, a spin current can also induce a transverse voltage drop, in an effect called the inverse SHE. Both the AHE and SHE are of particular interest for spintronic applications⁴⁻⁶ (and references therein) in which spin currents can be used to manipulate magnetic moments, for example, switching the state of magnetization of magnetic nano-elements, or for inducing the very efficient motion of domain walls^{7,8}. Thus, the SHE has recently attracted much attention by both experimentalists and theorists, and there has been widespread efforts to search for candidate materials that exhibit strong AHE or SHE.

The AHE and SHE originate from the electronic and magnetic structures of materials and have both extrinsic and intrinsic origins. Extrinsic contributions depend sensitively on impurity scattering while intrinsic effects are derived from properties of the band structure. It is the intrinsic AHE and SHE that are the subject of this article. For the AHE of an ordinary collinear ferromagnet, it has been established that the Berry curvature, a quantity closely determined by the band structure, acts as a fictitious magnetic field in momentum space, that is derived from the magnetization and SOC, and affects the

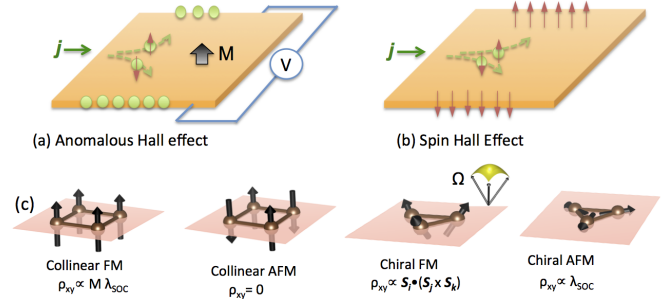


FIG. 1. Schematic illustrations of (a) the anomalous Hall effect and (b) the spin Hall effect from the viewpoint of spin-dependent Mott scattering. (c) The anomalous Hall effect in collinear FM, collinear AFM, chiral FM, and chiral AFM systems. ρ_{xy} , M , λ_{SOC} and $S_i \cdot (S_j \times S_k)$ represent the anomalous Hall resistivity, magnetization, strength of SOC and the scalar spin chirality, respectively.

charge motion in the same way as a real magnetic field⁹. In a collinear AFM, it is not surprising that the AHE vanishes due to the spin-up and -down conduction electron symmetry, or rather the existence of a symmetry by combining a time-reversal symmetry operation and a lattice translation. In a chiral ferromagnet where magnetic moments are tilted in a lattice, it was recently found that the aforementioned fictitious magnetic field can also be generated by the scalar spin chirality^{10,11}, $S_i \cdot (S_j \times S_k)$ ($S_{i,j,k}$ denote three non-coplanar spins), which does not necessarily involve SOC. When an electron makes a loop trajectory in a chiral FM lattice, the electron acquires a real-space Berry phase due to double exchange interactions with the chiral lattice spins. The corresponding AHE has been referred to as a so-called real-space topological Hall effect in the literature (e.g.¹²). In a chi-

ral AFM in which the magnetic moments are coplanar, the topological Hall effect disappears because of the zero spin chirality. However, an AHE can still exist due to a nonzero Berry curvature induced by the SOC¹³. Indeed, a strong AHE was recently observed in the chiral AFM compounds Mn₃Sn and Mn₃Ge^{13–16}. In principle, the SHE exists generically in systems with strong SOC. It has been studied

in nonmagnetic^{17–20} as well as antiferromagnetic^{20–24} metals. Very recently, a strong SHE was experimentally discovered in another chiral AFM compound Mn₃Ir²⁵. Therefore, chiral AFM materials are appealing candidates for finding significant AHE and SHE. They have also stimulated the search for Weyl points in the same family of materials²⁶ and exotic magneto-optical Kerr effect²⁷.

In this work, we have performed a comprehensive study of the intrinsic AHE and SHE of the compounds Mn₃X (X = Ge, Sn, Ga, Ir, Rh and Pt), using *ab initio* Berry phase calculations. These compounds exhibit a chiral AFM order well above room temperature (see Table I). This article is organized as follows. We first introduce the *ab initio* method and the linear-response method that we have used to compute the AHE and SHE in Sec. II. We then discuss the relationship of the symmetry of the crystal lattice and magnetic lattice to the SHC and AHC in

Sec. III. In Sec. IV, we discuss the results of our calculations with the assistance of symmetry analysis, where the Mn₃X compounds are classified into two groups according to their crystal and magnetic structures. Finally, we summarize our results in Sec. V.

II. METHODS

The anomalous Hall conductivity (AHC) and spin Hall conductivity (SHC) characterize the AHE and SHE, respectively. In addition, the spin lifetime and related spin manipulation methods are important ingredients for the SHE device applications, but these aspects are beyond the scope of the current study. The AHC and SHC have been calculated using the Berry phase that we have determined from *ab initio* band structures. Density-functional theory (DFT) calculations were performed for the Mn₃X bulk crystals with the Vienna *Ab – initio* Simulation Package (VASP)²⁸ within the generalized gradient approximation (GGA)²⁹. The SOC was included in our calculations. The material-specific Hamiltonians were established by projecting the DFT Bloch wave functions onto maximally localized Wannier functions (MLWFs)³⁰. Based on these tight-binding Hamiltonians, that include realistic material parameters, we have calculated the intrinsic AHC and SHC by using the Kubo formula approach within the linear response^{1,2,9,31}. The AHC ($\sigma_{\alpha\beta}$) is obtained from

$$\sigma_{\alpha\beta} = -\frac{e^2}{\hbar} \sum_n \int_{BZ} \frac{d^3\vec{k}}{(2\pi)^3} f_n(\vec{k}) \Omega_n(\vec{k}),$$

$$\Omega_n(\vec{k}) = 2i\hbar^2 \sum_{m \neq n} \frac{\langle u_n(\vec{k}) | \hat{v}_\alpha | u_m(\vec{k}) \rangle \langle u_m(\vec{k}) | \hat{v}_\beta | u_n(\vec{k}) \rangle}{(E_n(\vec{k}) - E_m(\vec{k}))^2},$$
(1)

where $\hat{v}_{\alpha(\beta,\gamma)} = \frac{i}{\hbar} [\hat{H}, \hat{r}_{\alpha(\beta,\gamma)}]$ is the velocity operator with $\alpha, \beta, \gamma = x, y, z$; \hat{r}_α is the position operator. $f_n(\vec{k})$ is the Fermi-Dirac distribution. $|u_n(\vec{k})\rangle$ and $E_n(\vec{k})$ are the eigenvector and eigenvalue of the Hamiltonian $\hat{H}(\vec{k})$, respectively. $\Omega_n(\vec{k})$ is the Berry curvature in momentum space, and the corresponding AHC $\sigma_{\alpha\beta}$ can be evaluated by summing the Berry curvature over the Brillouin zone (BZ) for all the occupied bands. Here $\sigma_{\alpha\beta}$ corresponds to a 3×3 matrix and indicates a transverse Hall current

j_α generated by a longitudinal electric field E_β , which satisfies $J_\alpha = \sigma_{\alpha\beta} E_\beta$. For the evaluation of the velocity operator we assume for simplicity that the position operator is diagonal in the Wannier basis, as is commonly done in tight-binding calculations.

The intrinsic SHC can be obtained by replacing the velocity operator with the spin current operator $\hat{J}_\alpha^\gamma = \frac{1}{2} \{\hat{v}_\alpha, \hat{s}_\gamma\}$, where \hat{s}_γ is the spin operator. The SHC then has the form of

$$\sigma_{\alpha\beta}^\gamma = \frac{e}{\hbar} \sum_n \int_{BZ} \frac{d^3\vec{k}}{(2\pi)^3} f_n(\vec{k}) \Omega_{n,\alpha\beta}^\gamma(\vec{k}),$$

$$\Omega_{n,\alpha\beta}^\gamma(\vec{k}) = 2i\hbar^2 \sum_{m \neq n} \frac{\langle u_n(\vec{k}) | \hat{J}_\alpha^\gamma | u_m(\vec{k}) \rangle \langle u_m(\vec{k}) | \hat{v}_\beta | u_n(\vec{k}) \rangle}{(E_n(\vec{k}) - E_m(\vec{k}))^2},$$
(2)

$\Omega_{n,\alpha\beta}^\gamma(\vec{k})$ is referred to as the spin Berry curvature in the following, in order to distinguish it from the Berry curvature $\tilde{\Omega}_n(\vec{k})$. The SHC ($\sigma_{\alpha\beta}^\gamma$; $\alpha, \beta, \gamma = x, y, z$) is a third-order tensor ($3 \times 3 \times 3$) and represents the spin current $J_s^\gamma_\alpha$ generated by an electric field \vec{E} via $J_s^\gamma_\alpha = \sigma_{\alpha\beta}^\gamma E_\beta$, where $J_s^\gamma_\alpha$ flows along the α -direction with the spin-polarization along the γ -direction and E_β is the β -component of the electric field \vec{E} .

For the integrals of Eqns. 1-2, the BZ was sampled by k -grids from $50 \times 50 \times 50$ to $200 \times 200 \times 200$. Satisfactory convergence was achieved for a k -grid of size $150 \times 150 \times 150$. Increasing the grid size to $200 \times 200 \times 200$ varied the SHC and AHC by no more than 5%. Note that the unit of SHC differs from that of the AHC by $\frac{\hbar}{2e}$, where $\hbar/2$ is the spin angular momentum and e is the electron charge. Thus, the unit of SHC is $(\hbar/e)(\Omega \cdot \text{cm})^{-1}$.

Since AHC and SHC are determined directly by the band structure, they are fully compatible with the symmetry of the Hamiltonian. Therefore, we can use symmetry analysis to simplify the shape of the AHC and SHC tensor matrices, by forcing certain matrix elements to be zero and constraining some to be the same. Here, we obtain the shape of the intrinsic response tensor from the Linear-Response-Symmetry code^{32,33}, which analyzes the symmetry operations of the corresponding crystal and magnetic space groups³⁴ and then determines the tensor shape by solving the linear equations. We note that a similar study³⁵ also recently considered how the shape of the tensor response varied according to the magnetic Laue group. The shape of the AHC and SHC tensors are shown in Table II. These are very helpful in checking the validity and numerical convergence of our calculations by comparing the symmetry of the calculated matrices and the ideal symmetry-imposed matrices. Furthermore, the tensor shape surely relies on the coordinate system that is specified in the next section. The AHC and SHC tensors can be expressed in different coordinate systems, which are physically equivalent, and can be transformed into each other according to specific rotation matrices³⁶.

III. CRYSTALLOGRAPHIC AND MAGNETIC STRUCTURES

The compounds considered here can be classified into two groups according to their crystallographic structure. Mn_3Ga , Mn_3Ge and Mn_3Sn display an hexagonal lattice with the space group $P6_3/mmc$ (No. 194). The primitive unit cell includes two Mn_3X planes that are stacked along the c axis according to “-AB-AB-”. Each structure contains plane of Mn atoms that constitute a Kagome-type lattice with Ga, Ge or Sn lying at the center of a hexagon formed from the Mn atoms. In the Kagome plane due to magneto-geometrical frustration, the Mn magnetic moments exhibit a non-collinear AFM order, where the neighboring moments are aligned at a 120° angle³⁷⁻³⁹. The energetically favored AFM configuration

was revealed, as illustrated in Fig. 2a, in earlier DFT calculations⁴⁰. The magnetic ordering temperatures are above 365 K for all these three compounds, as shown in Table I. Additionally, Mn_3Ga and Mn_3Ge can also crystallize into a tetragonal phase with a ferrimagnetic structure^{37,38,41}, which is not considered in this work.

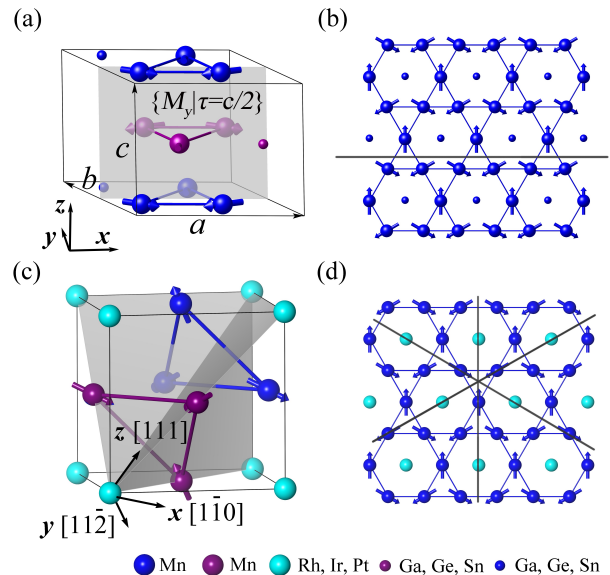


FIG. 2. Crystal lattice and magnetic structure for Mn_3X ($X = \text{Ga}, \text{Ge}, \text{Sn}, \text{Rh}, \text{Ir}, \text{Pt}$). (a) Mn_3X ($X = \text{Ga}, \text{Ge}$ and Sn) display an hexagon lattice with Mn forming a Kagome sublattice stacking along the c axis. The gray plane indicates the M_y mirror plane of the symmetry operation $\{M_y|\tau = c/2\}$. The crystallographic a and c axes align with the x and z directions, respectively, with the b axis lying inside the xy plane. (b) Top view of the Mn Kagome-type lattice showing triangular and hexagonal arrangements of the Mn moments. Arrows represent the Mn magnetic moments, presenting a non-collinear AFM configuration. The mirror plane position is indicated by a black line. (c) The crystal structure of Mn_3X ($X = \text{Rh}, \text{Ir}$ and Pt) has an FCC lattice. Three mirror planes are shown in gray. Here a mirror reflection combined with a time-reversal symmetry operation preserves the magnetic lattice. (d) The Mn sublattice also forms a Kagome-type configuration in Mn_3X ($X = \text{Rh}, \text{Ir}$ and Pt), thereby forming a non-collinear AFM phase, but which is slightly different from the Mn_3Ge family. The projections of three mirror planes are indicated by black lines. To match the hexagonal lattice conveniently, the Kagome plane is set as the xy plane and the plane normal as the z axis. Here x is along the crystallographic $[1\bar{1}0]$, y along $[11\bar{2}]$, and z along $[111]$.

Mn_3Rh , Mn_3Ir and Mn_3Pt crystallize in a face-centered cubic (FCC) lattice (space group $Pm\bar{3}m$, No. 221) with Ir (Rh, Pt) and Mn located at the corner and face-center sites, respectively, as shown in Fig. 2b. Within the (111) plane, the Mn sublattice also form a Kagome lattice. In contrast to that of Mn_3Ge , the

Kagome planes stack in an “-ABC-ABC-” sequence. The non-collinear AFM structure has also been observed by neutron diffraction measurements^{42–44}. Distinct from Mn_3Ge , here the magnetic moments all point towards or away from the center of the Mn triangles. The AFM order also persists to well above room temperature. (see Table I).

TABLE I. Crystal structure, magnetic structure and AFM ordering temperature (T_N) for Mn_3X compounds.

	T_N (K)	Crystal space group	Magnetic space group
Mn_3Ga^a	470		
Mn_3Ge^b	365	$P6_3/mmc$, no. 194	$R\bar{3}m'$
Mn_3Sn^c	420		
Mn_3Rh^d	853 ± 10		
Mn_3Ir^e	960 ± 10	$Pm\bar{3}m$, no. 221	$Am'm'm2$
Mn_3Pt^f	473 ± 10		

a, Ref. 37 *b*, Ref. 45 *c*, Ref. 46
d, Ref. 44 *e*, Ref. 43 *f*, Refs. 42 and 44

IV. RESULTS AND DISCUSSIONS

A. Anomalous Hall Effect in Mn_3Ga , Mn_3Ge and Mn_3Sn

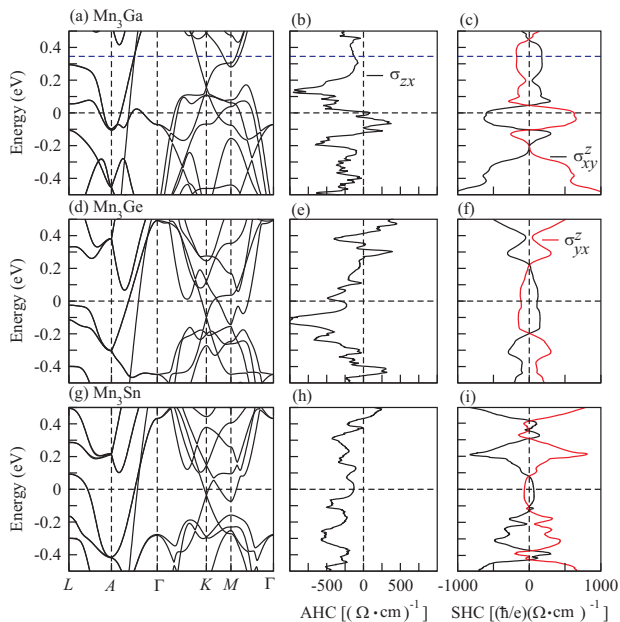


FIG. 3. Electronic band structure for (a) Mn_3Ga , (d) Mn_3Ge , and (g) Mn_3Sn . Energy dependent AHC σ_{zx} for (b) Mn_3Ga , (e) Mn_3Ge and (h) Mn_3Sn . Energy dependent SHC tensor elements of σ_{xy}^z and σ_{yx}^z for (c) Mn_3Ga , (f) Mn_3Ge , and (i) Mn_3Sn . Mn_3Ga would have the same number of valence electrons as does Mn_3Ge and Mn_3Sn if the Fermi level is shifted up to the blue dashed line in (a,b,c)

The AHC $\sigma_{\alpha\beta}$ can be understood by a consideration of the symmetry of the magnetic structure. As indicated in Fig. 1a there is a mirror plane \hat{M}_y that is parallel to the zx plane. By combining a mirror reflection about this plane and a translation operation along the c direction $\hat{\tau} = (0, 0, c/2)$, the system is imaged back onto itself with the same crystallographic and magnetic structures. Therefore, the magnetic structure in Mn_3Ga , Mn_3Ge and Mn_3Sn is symmetric with respect to the $\{\hat{M}_y|\hat{\tau}\}$ symmetry operator. The mirror operation \hat{M}_y changes the signs of $\Omega_{yz}(\vec{k})$ and $\Omega_{xy}(\vec{k})$, but preserves $\Omega_{zx}(\vec{k})$, since $\Omega_{\alpha\beta}(\vec{k})$ is a pseudovector, just like the spin. Accordingly, σ_{yz} and σ_{xy} that are parallel to the mirror plane are transformed to $-\sigma_{yz}$ and $-\sigma_{xy}$, with respect to the \hat{M}_y reflection (the translation operation does not affect the Berry curvature). Thus, from symmetry considerations, σ_{yz} and σ_{xy} must be zero, and only σ_{zx} can be nonzero. We therefore propose that the preferred experimental setup for maximizing AHC is to confine the electric field within the zx plane, for example, by setting the electric current along z and detecting the transverse voltage along x .

Our calculations are fully consistent with the above symmetry analysis, as shown in Table II, where only σ_{zx} ($\sigma_{xz} = -\sigma_{zx}$) is nonzero. The AHC of Mn_3Ge is as large as $330 (\Omega \cdot \text{cm})^{-1}$. Although Mn_3Sn has a stronger SOC than Mn_3Ge , its AHC is less than half that of Mn_3Ge . Mn_3Ga exhibits the smallest AHC and, moreover, the AHC has the opposite sign to those of the Ge and Sn compounds. This is fully consistent with recent experiments on the Ge and Sn compounds^{15,16}, where the in-plane AHC (σ_{xy}) is negligible compared to the out-of-plane AHC (σ_{zx} and σ_{yz}), and Mn_3Sn displays a smaller AHC in magnitude than Mn_3Ge . We note that σ_{zx} and σ_{yz} may be both nonzero if a different coordinate axis is chosen or the chiral moments are rotated by an external magnetic field.

Since the intrinsic AHE originates from the electronic band structure, we analyzed the band structure in detail to understand the differences among these three compounds. Their calculated band structures are shown in Fig. 3. Since the valence electrons for Ga and Ge (Sn) are $4s^24p^1$ and $4s^24p^2$ ($5s^25p^2$), respectively, the band structure of Mn_3Ga looks very similar to that of Mn_3Ge (Mn_3Sn). The Fermi level is shifted up by 0.34 eV (equivalent to adding one electron). Correspondingly, the shapes of the energy-dependent AHC curves for Mn_3Ga and Mn_3Ge (Mn_3Sn) are also very similar. The value of σ_{zx} in Mn_3Ga changes sign from negative to positive after tuning up the Fermi level.

Atomic Ge and Sn have similar valence electron configurations while Sn has a larger atomic radius and stronger SOC compared to Ge. Although the consequent changes in the band structures are subtle (see Fig. 3), the effect on the resultant AHC can be significant. To better understand the AHE in Mn_3Ge and Mn_3Sn , we considered the distributions of the Berry curvature in the reciprocal space. We have projected the Berry curvature components of Ω_{zx} onto the k_3 - k_1 (k_z - k_x) plane by in-

TABLE II. Shape of the AHC and SHC tensors obtained from symmetry analysis and numerical calculations for Mn_3X ($X=\text{Ga, Ge and Sn}$). The calculated SHC tensor elements are set to zero when they are smaller than $12 (\hbar/e)(\Omega \cdot \text{cm})^{-1}$. The coordinates used here are x along $[100]$, y along $[120]$, and z along $[001]$, as presented in Fig. 1(a, b). The AHC is given in units of $(\Omega \cdot \text{cm})^{-1}$ and the SHC in units of $(\hbar/e)(\Omega \cdot \text{cm})^{-1}$.

	AHC			SHC		
	σ	σ^x	σ^y	σ^z		
symmetry-imposed tensor shape	$\begin{pmatrix} 0 & 0 & -\sigma_{zx} \\ 0 & 0 & 0 \\ \sigma_{zx} & 0 & 0 \end{pmatrix}$	$\begin{pmatrix} 0 & 0 & 0 \\ 0 & 0 & \sigma_{yz}^x \\ 0 & \sigma_{zy}^x & 0 \end{pmatrix}$	$\begin{pmatrix} 0 & 0 & \sigma_{xz}^y \\ 0 & 0 & 0 \\ \sigma_{zx}^y & 0 & 0 \end{pmatrix}$	$\begin{pmatrix} 0 & \sigma_{xy}^z & 0 \\ \sigma_{yx}^z & 0 & 0 \\ 0 & 0 & 0 \end{pmatrix}$		
Mn_3Ga	$\begin{pmatrix} 0 & 0 & -81 \\ 0 & 0 & 0 \\ 81 & 0 & 0 \end{pmatrix}$	$\begin{pmatrix} 0 & 0 & 0 \\ 0 & 0 & -14 \\ 0 & 12 & 0 \end{pmatrix}$	$\begin{pmatrix} 0 & 0 & 15 \\ 0 & 0 & 0 \\ -7 & 0 & 0 \end{pmatrix}$	$\begin{pmatrix} 0 & -597 & 0 \\ 626 & 0 & 0 \\ 0 & 0 & 0 \end{pmatrix}$		
Mn_3Ge	$\begin{pmatrix} 0 & 0 & 330 \\ 0 & 0 & 0 \\ -330 & 0 & 0 \end{pmatrix}$	$\begin{pmatrix} 0 & 0 & 0 \\ 0 & 0 & -21 \\ 0 & 18 & 0 \end{pmatrix}$	$\begin{pmatrix} 0 & 0 & 21 \\ 0 & 0 & 0 \\ -18 & 0 & 0 \end{pmatrix}$	$\begin{pmatrix} 0 & 112 & 0 \\ -115 & 0 & 0 \\ 0 & 0 & 0 \end{pmatrix}$		
Mn_3Sn	$\begin{pmatrix} 0 & 0 & 133 \\ 0 & 0 & 0 \\ -133 & 0 & 0 \end{pmatrix}$	$\begin{pmatrix} 0 & 0 & 0 \\ 0 & 0 & -36 \\ 0 & 96 & 0 \end{pmatrix}$	$\begin{pmatrix} 0 & 0 & 36 \\ 0 & 0 & 0 \\ -96 & 0 & 0 \end{pmatrix}$	$\begin{pmatrix} 0 & 64 & 0 \\ -68 & 0 & 0 \\ 0 & 0 & 0 \end{pmatrix}$		

tegrating them along k_2 , where $k_{1,2,3}$ are the reciprocal lattice vectors, and k_3 and k_1 are aligned with the k_z and k_x axes, respectively. The projected Berry curvatures of Mn_3Ge and Mn_3Sn with the Fermi level lying at the charge neutral point are shown in Figs. 4(a) and 4(b), respectively. One can easily identify the origin of the significant differences of the Berry curvature between Mn_3Ge and Mn_3Sn . The large AHC mainly arises from the positive *hot spots* located around $(0.127, 0.428)$ (the coordinates are in units of the reciprocal lattice vectors k_1 and k_2) and its three partners in the k_3 - k_1 plane, while these four hot spots are not seen in Mn_3Sn . Taking the hotspot at $(0.127, 0.428)$ as an example, we have checked the band structure and corresponding Berry curvature evolution with k_2 varying from 0 to 1. From the band structure of Mn_3Ge in Fig. 4(c) we can see that the Fermi level crosses two small gaps around $k_2=0$ and 0.5. According to Eqn. 1, the entanglement between occupied and unoccupied states must be very strong around these two points and contributes to a large Berry curvatures, as indicated by the two peaks in Fig. 4(e). This is fully consistent with previous calculations on Mn_3Ge ¹⁶. Mn_3Sn has a similar band structure along the same k -path, as can be seen by comparing Fig. 4(c) and (d), whereas the band gaps around $k_2=0$ and 0.5 are much larger compared to that in Mn_3Ge . Consequently, the two Berry curvature peaks disappear in Mn_3Sn , as shown in Fig. 4(f). Thus, a tiny changes in band structure can result in significant changes in the Berry curvature and AHC in this class of compounds.

B. Spin Hall Effect in Mn_3Ga , Mn_3Ge and Mn_3Sn

By adding the spin degree of freedom, the SHC becomes a third-order tensor. Similar to the AHC, some SHC tensor elements will be exactly zero or will be identical based on the corresponding lattice and magnetic sym-

metries. The magnetic space group for Mn_3X ($X=\text{Ga, Ge and Sn}$) is identified to be $R\bar{3}m'$ and the corresponding Laue group is $m'm'm'$ ³⁴. The calculated shape of the intrinsic SHC tensor and corresponding numerical results are presented in Table II. Furthermore, the SHC of Mn_3X ($X=\text{Ga, Ge and Sn}$) is strongly anisotropic with dominant components of σ_{xy}^z and σ_{yx}^z . These results will provides helpful information for the experimental detection of the SHE. To illustrate the anisotropy of the SHC, we show the angle-dependent SHC for Mn_3Ge in Fig. 5. When the charge current J is fixed along x -axis (a direction) and by considering the spin current J_s perpendicular to J and rotating it, the corresponding magnitude of SHC is maximal for $J_s \parallel y$ while being zero for $J_s \parallel z$. Therefore, to observe large SHC, one should set the charge current and spin current inside the Kagome (xy) plane, for example with the electron current set along x and by measuring the transverse spin current along y with its spin polarization along z . Therefore, we stress that for optimizing the efficiency of devices that rely on SHE and AHE, the direction of the charge current and the resulting spin current will depend on the respective compound.

As shown in Table II, the largest SHCs σ_{xy}^z and σ_{yx}^z are of the order of $120 (\hbar/e)(\Omega \cdot \text{cm})^{-1}$ in magnitude for Mn_3Ge . With the relatively small electrical conductivity (about $3300 (\Omega \cdot \text{cm})^{-1}$), we would have a spin Hall angle up to 3%. Also the σ_{yx}^z elements in Mn_3Ga is around 600 $(\hbar/e)(\Omega \cdot \text{cm})^{-1}$. Additionally, it is not surprising that σ_{xy}^z and σ_{yx}^z are not equal in magnitude, for the x and y directions are not equivalent in a Kagome structure.

Since the SHC is strongly related to the location of the Fermi level, the SHC varies quickly as the Fermi energy is shifted, especially for the metallic band structures shown in Fig. 3. The energy-dependent SHC of the most prominent tensor elements σ_{xy}^z and σ_{yx}^z for the three compounds are shown in Figs. 3 (e), (f) and (i). Owing to the similar crystal lattice constant and the same magnetic or-

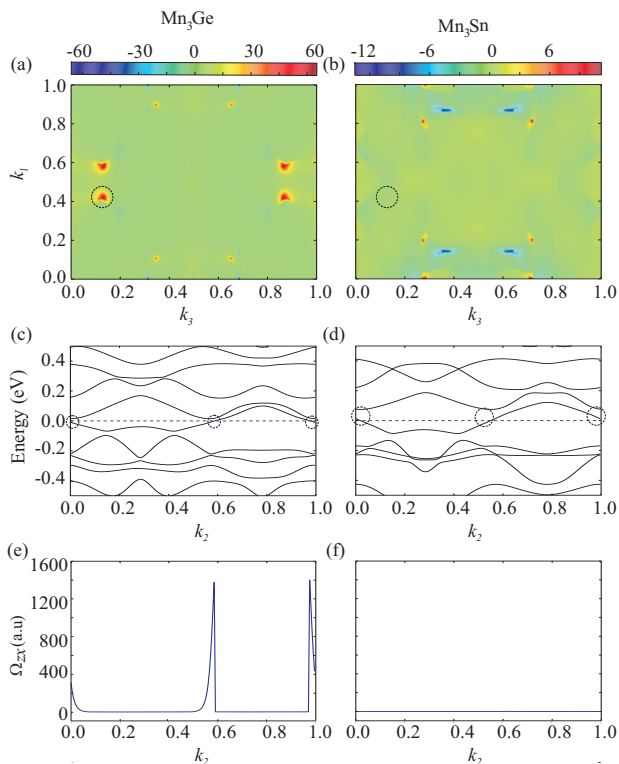


FIG. 4. (a, b) Berry curvature projected onto the k_3 - k_1 plane for Mn_3Ge and Mn_3Sn , respectively. The Berry curvature in Mn_3Ge is dominated by the four areas that are highlighted in yellow in (a). (c) Energy dispersion of Mn_3Ge along k_2 with (k_3, k_1) fixed at the Berry curvature dominated point (0.127, 0.428), identified as the black dashed circle marked in (a). The band gaps are very small near $k_2=0.5$ and 1, which are noted by the small black dashed circles. (d) Band structure of Mn_3Sn for the same reciprocal space cut as in (c). The band gaps are much larger in Mn_3Sn , as denoted by the larger black dashed circles. (e) The evolution of the Berry curvature Ω^y of Mn_3Ge corresponding to the band structure given in (c). The small band gaps around $k_2=0.5$ and 1 make larger contributions to the Berry curvature. (f) The magnitude of Berry curvature along the same path in Mn_3Sn is negligibly small compared to that in Mn_3Ge .

der, the shapes of the SHC curves are very similar, if we ignore the fact that Ga has one electron less than either Ge or Sn. For Mn_3Ga , the SHC exhibits a minimum at the Fermi level, the charge neutral point, and increases quickly if the Fermi level moves up or down. Hence an even larger SHC is expected for Mn_3Ga with small electron or hole doping. One can see that the SHC remains relatively stable with respect to varying the Fermi level in the energy window of ± 0.1 eV for Mn_3Ge and Mn_3Sn . Thus indicates that the SHC in the Ge and Sn compounds is robust.

Since the spin Berry curvature is distinct from the Berry curvature, the SHC and AHC can have dominant contributions from different electronic bands. Although Mn_3Ge and Mn_3Sn display very different AHCs in mag-

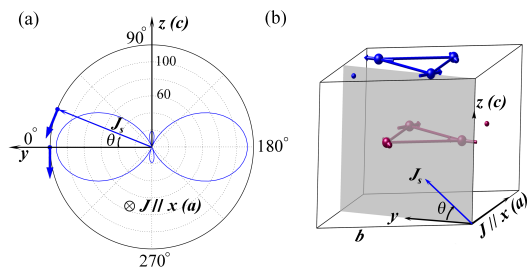


FIG. 5. (a) Angle-dependent spin current J_s arising from a charge current J along the x axis (the crystallographic a lattice vector) in Mn_3Ge . J_s rotates inside the yz plane. The largest spin Hall conductivity is when J_s is along the y axis ($\theta = 0^\circ$). The blue arrows represent the spin polarization directions of J_s . (b) Schematic of J_s and J with respect to the lattice orientation.

nitude, their SHCs are very close. Therefore, we expect a similar spin Berry curvature distribution in k space for both compounds. Taking the components of Ω_{xy}^z as an example, we compare the spin Berry curvature distributions for Mn_3Ge and Mn_3Sn with the Fermi energy lying at the charge neutral point. Similar to the above analysis for the AHE, we also project the spin Berry curvature onto the $k_3 - k_1$ plane by integrating Ω_{xy}^z along k_2 . As shown in Fig. 6, Mn_3Ge and Mn_3Sn display similar features in their respective spin Berry curvature distributions. The shapes of the dominant areas are very similar in both compounds, with just a little shift within the $k_3 - k_1$ plane. The dominant contribution forms thick arcs with a transition point between positive and negative amplitudes, where the integrated spin Berry curvature transfers from positive to negative. Since the size of the positive dominant area is much larger than that of the negative part, the integral of the spin Berry curvature in the whole BZ gives a positive SHC σ_{xy}^z , as is listed in Table II.

The above positive-negative spin Berry curvature distribution is reminiscent of the similar feature of the SHE around Weyl point, where positive and negative spin Berry curvature appear with the Weyl point as the transition point²⁶. In fact Weyl points also exist in Mn_3Ge and Mn_3Sn , however, the spin Berry curvature transition point in Fig. 6 does not exactly overlap with the Weyl point. A careful inspection of the band dispersions along k_2 through these hot spots reveals tiny band gaps that contribute to the peaks of the spin Berry curvature, as shown in Figs. 6 (e) and (f). Therefore, the intrinsic SHC mainly arises from the small band gaps lying very close to the Fermi level.

TABLE III. The intrinsic AHC and SHC tensors obtained from symmetry analysis and numerical calculations for Mn_3X ($X = \text{Rh, Ir and Pt}$). The calculated SHC tensor elements are set to zero when they are smaller than $5 (\hbar/e)(\Omega \cdot \text{cm})^{-1}$. The coordinate axes correspond to z oriented in the $[111]$ direction, x along $[\bar{1}\bar{1}0]$ and y along $[1\bar{1}\bar{2}]$. The AHC is in units of $(\Omega \cdot \text{cm})^{-1}$ and the SHC is in units of $(\hbar/e)(\Omega \cdot \text{cm})^{-1}$.

	AHC		SHC			
	σ	σ^x	σ^y		σ^z	
symmetry-imposed tensor shape	$\begin{pmatrix} 0 & \sigma_{xy} & 0 \\ -\sigma_{xy} & 0 & 0 \\ 0 & 0 & 0 \end{pmatrix}$	$\begin{pmatrix} \sigma_{xx}^x & 0 & 0 \\ 0 & -\sigma_{xx}^x & \sigma_{yz}^x \\ 0 & \sigma_{zy}^x & 0 \end{pmatrix}$	$\begin{pmatrix} 0 & -\sigma_{xx}^x & -\sigma_{yz}^x \\ -\sigma_{xx}^x & 0 & 0 \\ -\sigma_{zy}^x & 0 & 0 \end{pmatrix}$		$\begin{pmatrix} 0 & \sigma_{xy}^z & 0 \\ -\sigma_{xy}^z & 0 & 0 \\ 0 & 0 & 0 \end{pmatrix}$	
Mn_3Rh	$\begin{pmatrix} 0 & -284 & 0 \\ 284 & 0 & 0 \\ 0 & 0 & 0 \end{pmatrix}$	$\begin{pmatrix} -276 & 0 & 0 \\ 0 & 276 & 220 \\ 0 & 70 & 0 \end{pmatrix}$	$\begin{pmatrix} 0 & 276 & -220 \\ 276 & 0 & 0 \\ -70 & 0 & 0 \end{pmatrix}$		$\begin{pmatrix} 0 & 145 & 0 \\ -145 & 0 & 0 \\ 0 & 0 & 0 \end{pmatrix}$	
Mn_3Ir	$\begin{pmatrix} 0 & -312 & 0 \\ 312 & 0 & 0 \\ 0 & 0 & 0 \end{pmatrix}$	$\begin{pmatrix} -210 & 0 & 0 \\ 0 & 210 & 299 \\ 0 & -7 & 0 \end{pmatrix}$	$\begin{pmatrix} 0 & 210 & -299 \\ 210 & 0 & 0 \\ 7 & 0 & 0 \end{pmatrix}$		$\begin{pmatrix} 0 & 163 & 0 \\ -163 & 0 & 0 \\ 0 & 0 & 0 \end{pmatrix}$	
Mn_3Pt	$\begin{pmatrix} 0 & 98 & 0 \\ -98 & 0 & 0 \\ 0 & 0 & 0 \end{pmatrix}$	$\begin{pmatrix} -66 & 0 & 0 \\ 0 & 66 & 108 \\ 0 & 7 & 0 \end{pmatrix}$	$\begin{pmatrix} 0 & 66 & -108 \\ 66 & 0 & 0 \\ -7 & 0 & 0 \end{pmatrix}$		$\begin{pmatrix} 0 & 32 & 0 \\ -32 & 0 & 0 \\ 0 & 0 & 0 \end{pmatrix}$	

C. Anomalous Hall effect and spin Hall effect in Mn_3Rh , Mn_3Ir and Mn_3Pt

In the cubic lattice of Mn_3Rh , Mn_3Ir and Mn_3Pt , there are three mirror planes that intersect the crystallographic $[111]$ axis and which are related to each other by a three-fold rotation. The mirror reflection \hat{M} preserves the lattice symmetry but reverses all spins in the Kagome plane. Since time-reversal symmetry \hat{T} can also reverse spins, the combined symmetry of time-reversal and mirror symmetry, $\hat{T}\hat{M}$ is the symmetry of the system. $\hat{T}\hat{M}$ forces the out-of-mirror-plane AHC components to be zero, since the out-of-plane Berry curvature is odd with respect to \hat{T} but even with respect to \hat{M} . Given the existence of the three mirror planes, the only nonzero AHC component is along the co-axis of these three planes, i.e. the $[111]$ axis. For the convenience of the symmetry analysis, we used coordinates with z along the $[111]$ direction and x, y within the Kagome plane (see Fig. 1).

Our numerical calculations are again consistent with the symmetry analysis. The AHC for Mn_3Ir can reach $\sigma_{xy} = 312(\Omega \cdot \text{cm})^{-1}$ with the electric field lying in the (111) plane, as presented in Table III, which agrees with previous calculations¹³. Compared to Mn_3Ir , Mn_3Rh exhibits similar AHC in magnitude while Mn_3Pt shows a much smaller AHC. Mn_3Rh and Mn_3Ir show very similar trends in the Fermi-energy-dependent AHC, as shown in Figs. 7(b) and (e). The peak values appear around 50 meV above the charge neutral point for both Mn_3Rh and Mn_3Ir . Therefore, in order to get strong AHE, one simply needs weak electron doping, and the AHC in the (111) plane can then reach 450 and 500 $(\Omega \cdot \text{cm})^{-1}$ for Mn_3Rh and Mn_3Ir , respectively. Compared to Rh and Ir, Pt has one more valence electron. Hence the Mn_3Pt can be viewed as a strongly doped version of Mn_3Ir , which shifts the Fermi level a little further beyond the peak values, leading to a small AHC of 98 $(\Omega \cdot \text{cm})^{-1}$, as shown in Fig. 7(h).

The magnetic space group for Rh, Ir and Pt compounds is $Am'm'm2$, from which we can obtain the symmetry of the SHC tensor. As shown in Table III, there are only four independent nonzero elements. Our numerical calculations fit the symmetry-imposed tensor shape very well, as shown in Table III. The largest SHC tensor elements are σ_{yz}^x ($\sigma_{xz}^y = \sigma_{yz}^x$) and σ_{xy}^y ($\sigma_{yx}^y = \sigma_{yx}^y = -\sigma_{xx}^x = \sigma_{yy}^x$) for Mn_3Rh and Mn_3Ir . Therefore, the optimal experimental arrangement for large SHC is to align J_s within the xy plane [the (111) Kagome plane]. It is interesting that J, J_s and the spin polarization of J_s are not necessarily perpendicular to each other and even can be parallel, as indicated by the nonzero σ_{xx}^x . The large value of σ_{xx}^x shows a longitudinal spin current J_s induced by a charge current J along the same direction. Such a longitudinal spin current is common in FM metals where conduction electrons are naturally spin-polarized. However, it is interesting that these three AFM compounds can generate a similar spin current, which may promise novel spintronic applications. In previous experiments on Mn_3Ir ²⁵, the spin current was measured in two cases where the charge current was fixed along the $[\bar{1}\bar{1}0]$ crystallographic direction (i.e. x axis of the current work), J_s along the $[111]$ (i.e. z axis) direction and the $[001]$ direction. The former case was found to exhibit a much smaller SHE than the latter one. Therefore, we calculate the angle-dependent SHC by fixing $J||x$ and rotating J_s in the yz plane for Mn_3Ir , as shown in Fig. 8. One clearly sees that the SHC is only 7 $(\hbar/e)(\Omega \cdot \text{cm})^{-1}$ for the former case ($\theta = 0^\circ$) and 215 $(\hbar/e)(\Omega \cdot \text{cm})^{-1}$ for the latter case ($\theta = 144.7^\circ$).

Similar to the AHC, the peak values of σ_{xx}^x and σ_{yz}^x also appear around 50 meV above the charge neutral point for Mn_3Rh and Mn_3Ir , while their σ_{xy}^z is quite small. In contrast, the Fermi-energy-dependent AHC of Mn_3Pt shows a similar shape to that of the Rh and Ir compounds but the corresponding Fermi energy should be upshifted by one additional electron, as shown in Fig. 7(i). Thus, it is not surprising that σ_{xy}^z shows a large magnitude at

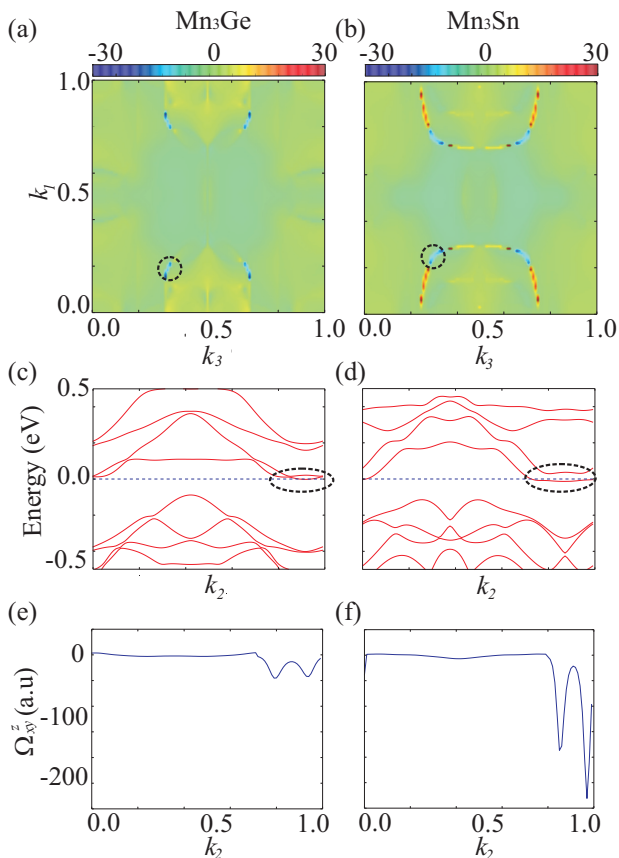


FIG. 6. (a, b) Spin Berry curvature projected onto the k_3 - k_1 plane for Mn_3Ge and Mn_3Sn , respectively. The two compounds have similar distributions of the projected spin Berry curvature. (c, d) Band structures of Mn_3Ge and Mn_3Sn , respectively, along k_2 . The coordinates of k_3 and k_1 are fixed at (0.31, 0.15) and (0.29, 0.24) for Mn_3Ge and Mn_3Sn , respectively, as noted by the black dashed circles in (a) and (b). Small band gaps exist around the $k_2=1$ point for both Mn_3Ge and Mn_3Sn , as marked by the black dashed circles. (e, f) Corresponding spin Berry curvature evolutions along k_2 for Mn_3Ge and Mn_3Sn , respectively. The large spin Berry curvature mainly originates from the small band gaps in the band structures.

the charge neutral point for Mn_3Pt .

V. SUMMARY

In summary, we have studied the intrinsic AHE and SHE in the non-collinear AFM compounds Mn_3X ($X = \text{Ge}, \text{Sn}, \text{Ga}, \text{Rh}, \text{Ir}, \text{and Pt}$) by *ab initio* calculations. Large AHC and large SHC are found for these materials, which are also highly anisotropic and in agreement with recent experimental measurements. Such an anisotropy is closely related to the symmetry of the AFM Kagome lattice, which can be helpful in rationalizing the numerical results. Based on our calculations, we have proposed the optimal experimental setups to maximize

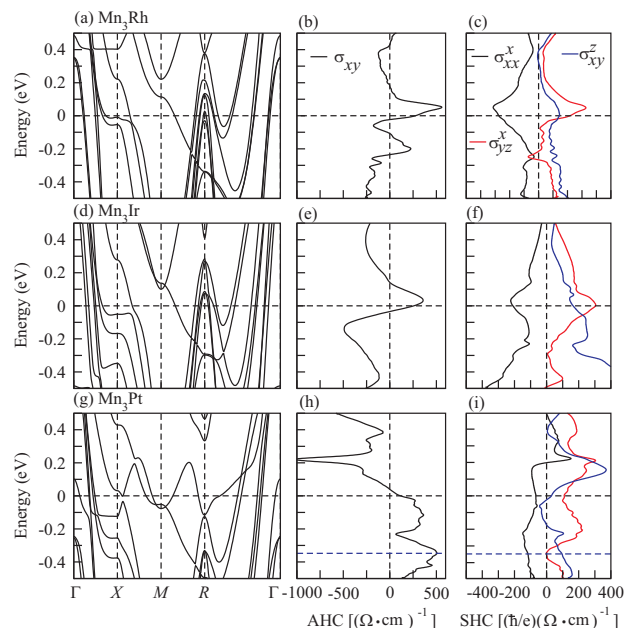


FIG. 7. Electronic band structure for (a) Mn_3Rh , (d) Mn_3Ir , and (g) Mn_3Pt . Energy dependent AHC element of σ^z for (b) Mn_3Rh , (e) Mn_3Ir and (h) Mn_3Pt . Energy dependent SHC tensor elements σ_{xx}^x , σ_{yz}^x and σ_{xy}^z for (c) Mn_3Rh , (f) Mn_3Ir , and (i) Mn_3Pt . Mn_3Pt would have the same number of valence electrons as Mn_3Rh and Mn_3Ir if the Fermi level shifts down to the blue dashed line in (g,h,i)

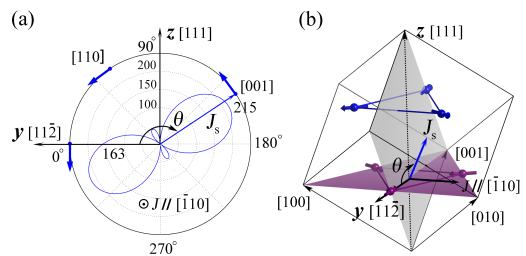


FIG. 8. (a) Angle-dependent spin Hall conductivity for Mn_3Ir . The charge current J flows along x (i.e. $[\bar{1}\bar{1}0]$) and the resulting spin current J_s is shown in the yz plane. The SHC is largest when $J_s \parallel [001]$ and smallest when $J_s \parallel [111]$. (b) Schematic of J and J_s within the crystal structure.

the AHE and SHE for different systems, as shown in Table IV. Although the SOC magnitude increases from Rh, to Ir and to Pt, the magnitude of the corresponding AHC and SHC do not follow the same trend. This is also true for the Ga, Ge, and Sn compounds. This indicates that the electron filling and the detailed band structures are essential in determining the magnitude of the AHE and SHE. We point out that the largest SHC attains a value of around $600 (\hbar/e)(\Omega \cdot \text{cm})^{-1}$ in Mn_3Ga . Our work provides insights in the interpretation and realization of a strong AHE and SHE in chiral AFM materials.

TABLE IV. Summary of the optimal experimental arrangements to realize large AHE and SHE. The xy plane refers to the Kagome AFM plane and the z direction is perpendicular to this plane. For AHE, the preferred plane to set the current and detect the Hall voltage is specified. For SHE, the charge current J and spin current J_s directions, which are supposed to be orthogonal, are indicated.

	AHE	SHE
Mn ₃ Ga		
Mn ₃ Ge	xz plane	xy plane
Mn ₃ Sn		
Mn ₃ Rh		
Mn ₃ Ir	xy plane	J_s inside the xy plane
Mn ₃ Pt		

ACKNOWLEDGMENTS

We thank Jario Sinova, Jereon van den Brink, and Carsten Timm for helpful discussions. C.F. acknowledges the funding support by ERC (Advanced Grant No. 291472 "Idea Heusler"). Y.Z. and B.Y. acknowledge the German Research Foundation (DFG) SFB 1143.

- * yan@cps.mpg.de
- ¹ N. Nagaosa, J. Sinova, S. Onoda, A. H. MacDonald, and N. P. Ong, *Reviews of Modern Physics* **82**, 1539 (2010).
 - ² J. Sinova, S. O. Valenzuela, J. Wunderlich, C. Back, and T. Jungwirth, *Reviews of Modern Physics* **87** (2015).
 - ³ M. Dyakonov and V. Perel, *Physics Letters A* **35**, 459 (1971).
 - ⁴ T. Jungwirth, J. Wunderlich, and K. Olejník, *Nature Materials* **11**, 382 (2012).
 - ⁵ S. Maekawa, S. O. Valenzuela, E. Saitoh, and T. Kimura, *Spin Current*, Vol. 17 (Oxford University Press, 2012).
 - ⁶ A. Hoffmann, *IEEE TRANSACTIONS ON MAGNETICS* **49**, 5172 (2013).
 - ⁷ S. Parkin and S.-H. Yang, *Nature Nanotech* **10**, 195 (2015).
 - ⁸ S.-H. Yang, K.-S. Ryu, and S. Parkin, *Nature Nanotech* **10**, 221 (2015).
 - ⁹ D. Xiao, M.-C. Chang, and Q. Niu, *Rev. Mod. Phys.* **82**, 1959 (2010).
 - ¹⁰ K. Ohgushi, S. Murakami, and N. Nagaosa, *Physical Review B* **62**, R6065 (2000).
 - ¹¹ Y. Taguchi, Y. Oohara, H. Yoshizawa, N. Nagaosa, and Y. Tokura, *Science* **291**, 2573 (2001).
 - ¹² A. Neubauer, C. Pfleiderer, B. Binz, A. Rosch, R. Ritz, P. G. Niklowitz, and P. Böni, *Phys. Rev. Lett.* **102**, 186602 (2009).
 - ¹³ H. Chen, Q. Niu, and A. MacDonald, *Phys. Rev. Lett.* **112**, 017205 (2014).
 - ¹⁴ J. Kübler and C. Felser, *EPL* **108**, 67001 (2014).
 - ¹⁵ S. Nakatsui, N. Kiyohara, and T. Higo, *Nature* **527**, 212 (2015).
 - ¹⁶ A. K. Nayak, J. E. Fischer, Y. Sun, B. Yan, J. Karel, A. C. Komarek, C. Shekhar, N. Kumar, W. Schnelle, J. Kuebler, C. Felser, and S. S. P. Parkin, *Science Advances* **2**, 150187 (2016).
 - ¹⁷ G. Y. Guo, S. Murakami, T.-W. Chen, and N. Nagaosa, *Phys. Rev. Lett.* **100**, 096401 (2008).
 - ¹⁸ T. Tanaka, H. Kontani, M. Naito, T. Naito, D. S. Hirashima, K. Yamada, and J. Inoue, *Phys. Rev. B* **77**, 165117 (2008).
 - ¹⁹ F. Freimuth, S. Blügel, and Y. Mokrousov, *Phys. Rev. Lett.* **105**, 246602 (2010).
 - ²⁰ B. Zimmermann, K. Chadova, D. Kodderitzsch, S. Blügel, H. Ebert, D. V. Fedorov, N. H. Long, P. Mavropoulos, I. Mertig, Y. Mokrousov, and M. Gradhand, *Phys. Rev. B* **90**, 220403 (2014).
 - ²¹ S. Fukami, C. Zhang, S. DuttaGupta, A. Kurenkov, and H. Ohno, *Nature materials* (2016).
 - ²² Y.-W. Oh, S.-h. C. Baek, Y. Kim, H. Y. Lee, K.-D. Lee, C.-G. Yang, E.-S. Park, K.-S. Lee, K.-W. Kim, G. Go, *et al.*, *Nature Nanotechnology* (2016).
 - ²³ V. Tshitoyan, C. Ciccarelli, A. Mihai, M. Ali, A. Irvine, T. Moore, T. Jungwirth, and A. Ferguson, *Physical Review B* **92**, 214406 (2015).
 - ²⁴ W. Zhang, M. B. Jungfleisch, W. Jiang, J. E. Pearson, A. Hoffmann, F. Freimuth, and Y. Mokrousov, *Physical review letters* **113**, 196602 (2014).
 - ²⁵ W. Zhang, W. Han, S. H. Yang, Y. Sun, Y. Zhang, B. Yan, and S. Parkin, *Science Advances* **2**, e1600759 (2016).
 - ²⁶ H. Yang, Y. Sun, Y. Zhang, W.-J. Shi, S. S. P. Parkin, and B. Yan, arXiv:1608.03404 (2016).
 - ²⁷ W. Feng, G.-Y. Guo, J. Zhou, Y. Yao, and Q. Niu, *Phys. Rev. B* **92**, 144426 (2015).
 - ²⁸ G. Kresse and J. Furthmüller, *Phys. Rev. B* **54**, 11169 (1996).
 - ²⁹ J. P. Perdew, K. Burke, and M. Ernzerhof, *Phys. Rev. Lett.* **77**, 3865 (1996).
 - ³⁰ A. A. Mostofi, J. R. Yates, Y.-S. Lee, I. Souza, D. Vanderbilt, and N. Marzari, *Comput. Phys. Commun.* **178**, 685 (2008).
 - ³¹ M. Gradhand, D. Fedorov, F. Pientka, P. Zahn, I. Mertig, and B. L. Györfy, *Journal of Physics: Condensed Matter* **24**, 213202 (2012).
 - ³² J. Železný, H. Gao, A. Manchon, F. Freimuth, Y. Mokrousov, J. Zemen, J. Mašek, J. Sinova, and T. Jungwirth, *Phys. Rev. B* **95**, 014403 (2017).
 - ³³ <https://bitbucket.org/zeleznyj/linear-response-symmetry>.
 - ³⁴ ISOTROPY Software Suite, iso.byu.edu.
 - ³⁵ M. Seemann, D. Koedderitzsch, S. Wimmer, and H. Ebert, *Physical Review B* **92**, 155138 (2015).
 - ³⁶ W. H. Kleiner, *Physical Review* **142** (1966).
 - ³⁷ E. Krén and G. Kádár, *Solid State Communications* **8**, 1653 (1970).
 - ³⁸ G. Kádár and E. Krén, *International Journal of Magnetism* **1**, 43 (1971).
 - ³⁹ T. Ohoyama, K. Yasukuchi, and K. Kanematsu, *Phys. Soc. Japan* **16**, 325 (1961).

- ⁴⁰ D. Zhang, B. Yan, S.-C. Wu, J. Kübler, G. Kreiner, S. S. Parkin, and C. Felser, *Journal of Physics: Condensed Matter* **25**, 206006 (2013).
- ⁴¹ B. Balke, G. H. Fecher, J. Winterlik, and C. Felser, *Appl. Phys. Lett.* **90**, 152504 (2007).
- ⁴² E. Krén, G. Kádár, L. Pál, J. Sólyom, P. Szabó, and T. Tarnóczy, *Physical review* **171**, 574 (1968).
- ⁴³ I. Tomeno, H. N. Fuke, H. Iwasaki, M. Sahashi, and Y. Tsunoda, *Journal of applied physics* **86**, 3853 (1999).
- ⁴⁴ E. Krén, G. Kádár, L. Pál, J. Sólyom, and P. Szabó, *Physics Letters* **20**, 331 (1966).
- ⁴⁵ N. Yamada, H. Sakai, H. Mori, and T. Ohoyama, *Physica B+ C* **149**, 311 (1988).
- ⁴⁶ J. Sticht, K. Höck, and J. Kübler, *Journal of Physics: Condensed Matter* **1**, 8155 (1989).